ORIGINAL STUDY

Gravity field modelling in mountainous areas by solving the nonlinear satellite-fixed geodetic boundary value problem with the finite element method

Marek Macák[1] · **Zuzana Minarechová**[1] · **Róbert Čunderlík**[1] · **Karol Mikula**[1,2]

Abstract

The paper concerns a novel concept based on the iterative approach applied for solving the nonlinear satellite-fixed geodetic boundary value problem (NSFGBVP) using the finite element method (FEM). We formulate the NSFGBVP that consists of the Laplace equation defined in the 3D bounded domain outside the Earth, the nonlinear boundary condition (BC) prescribed on the disretized Earth's surface, and the Dirichlet BC given on a spherical boundary placed approximately at the altitude of GOCE satellite mission and additional four side boundaries. The iterative approach is based on determining the direction of actual gravity vector together with the value of the disturbing potential. Such a concept leads to the first iteration where the oblique derivative boundary value problem is solved, and the last iteration represents the approximation of the actual disturbing potential and the direction of gravity vector. As a numerical method for our approach, we implement the FEM with triangular prisms. High-resolution numerical experiments deal with the local gravity field modelling in the Andean, Himalayan and Alpine mountain range, where we focus on the contribution to the disturbing potential solution by solving the nonlinear geodetic boundary value problem in comparison with the solution to the oblique derivative geodetic boundary value problem. The obtained results showed the maximal contribution of the presented approach 0.0571 [m^2s^{-2}] (Andes), 0.0702 [m^2s^{-2}] (Himalayas), 0.0066 [m^2s^{-2}] (Alps) in the disturbing potential, that is located in the areas of the highest values of the deflection of vertical.

1 Introduction

The nonlinear boundary value problems (BVPs) arise in a variety of areas of engineering tasks, and in our study we will focus on those that concern the gravity field modelling. The first application of a nonlinear BVP for the Laplace equation to gravity was given by Backus in Backus (1968). Then Grafarend and Niemeier discussed the free nonlinear BVP exactly solved by metric continuation in Grafarend and Niemeier (1971), and developed and extended

---

this approach in the report published by Grafarend in Grafarend (1989). Koch and Pope (1972) presented a uniqueness proof for the nonlinear geodetic BVP. Few years later Bjerhammar and Svensson (1983) used the general implicit function theorem and gave a solution of the existence and uniqueness problem in the nonlinear case. An interesting study discussing an expansion of the nonlinear boundary condition into a Taylor series, based upon some reference potential field approximating the geopotential, was shown by Heck in Heck (1989). In the same year, Sacerdote and Sansó (1989) further developed the idea used by Bjerhammar and Svensson for an iterative solution and they found explicit convergence conditions. They calculated the respective constant governing the convergence in the ideal case of a spherical boundary. Díaz et al. (2006, 2011) showed the existence and uniqueness of a viscosity solution for the Backus problem. Recently, Macák et al. (2016) published a numerical approach for solving the nonlinear satellite-fixed geodetic boundary value problem (NSFGBVP) by the finite volume method (FVM).

In this paper, we solve the same NSFGBVP as defined in Macák et al. (2016), however, for its solution, we implement the finite element method (FEM) and apply it to a very detailed local gravity field modelling in Andean, Himalayan and Alpine mountain ranges using large-scale parallel computations. Moreover, in this approach we use the triangular discretization of the bottom boundary, which is natural for approximating the complicated Earth's surface, while in Macák et al. (2016) only ellipsoidal approximation has been applied. In this way, we utilize the main advantages of numerical approaches applied to gravity field modelling, such as a straightforward refinement of the discretization, opportunity to consider real complicated topography as well as feasibility for high-resolution modelling. We expect that taking into account the proposed iterative procedure will improve the solution in the areas of the highest values of the deflection of vertical.

The paper is organized as follows. In the Sect. 2, we formulate the NSFGBVP and derive the iterative procedure for our approach. In the Sect. 3, we present its solution by the FEM using the pentahedral elements (i.e. triangular prisms). The Sect. 5 deals with the high-resolution local gravity field modelling and presents a discussion on the obtained results. The paper ends with conclusion and summary.

2 Formulation of the nonlinear satellite-fixed geodetic boundary value problem and the iterative procedure

Let us consider the bounded domain Ω depicted in Fig. 1, similarly as it was defined in Fašková et al. (2007, 2010). The domain Ω is placed in the external space above the Earth and is bounded by the bottom surface Γ representing a chosen part of the Earth's surface, the corresponding upper part of the boundary at altitude of the GOCE satellite mission and additional four side boundaries.

In the Ω domain, we suppose the nonlinear satellite-fixed geodetic BVP (NSFGBVP) for the disturbing potential $T(\mathbf{x})$ that was defined in Macák et al. (2016) and is formulated in the following form

$$\Delta T(\mathbf{x}) = 0 \quad \mathbf{x} \in \Omega, \tag{1}$$

$$|\nabla(T(\mathbf{x}) + U(\mathbf{x}))| = g(\mathbf{x}) \quad \mathbf{x} \in \Gamma, \tag{2}$$

$$T(\mathbf{x}) = T_{SAT}(\mathbf{x}) \quad \mathbf{x} \in \partial\Omega - \Gamma. \tag{3}$$

Fig. 1 Brief sketch of the computational domain Ω (highlighted in blue) for the local gravity field modelling. The boundary Γ, visualised by green hatching, represents the approximation of the chosen part of the Earth's surface, B and L denote ellipsoidal latitude and longitude, respectively
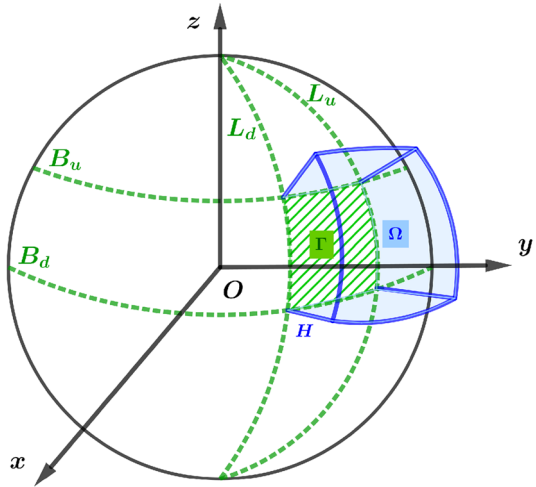
where $U(\mathbf{x})$ denotes the normal gravity potential (Hofmann-Wellenhof and Moritz 2006), $g(\mathbf{x})$ the magnitude of total gravity vector and T_{SAT} is, in general, the disturbing potential generated from a satellite-only global geopotential model (GGM) based on the spherical harmonics. The Eq. 2) represents the nonlinear boundary condition (BC).

The derivation of the iterative procedure has been published in Macák et al. (2016), but since it is very crucial for better understanding as well as readability of this paper, we present the main ideas also here.

We rewrite the norm of the gradient on the left-hand side of BC (2) in the form

$$|\nabla(T(\mathbf{x}) + U(\mathbf{x}))| = \frac{\nabla(T(\mathbf{x}) + U(\mathbf{x}))}{|\nabla(T(\mathbf{x}) + U(\mathbf{x}))|} \cdot \nabla(T(\mathbf{x}) + U(\mathbf{x})) \tag{4}$$

and insert (4) into (2) to obtain

$$\frac{\nabla(T(\mathbf{x}) + U(\mathbf{x}))}{|\nabla(T(\mathbf{x}) + U(\mathbf{x}))|} \cdot \nabla(T(\mathbf{x}) + U(\mathbf{x})) = g(\mathbf{x}). \tag{5}$$

If we denote by $\mathbf{v}(\mathbf{x})$ the unit vector

$$\mathbf{v}(\mathbf{x}) = \frac{\nabla(T(\mathbf{x}) + U(\mathbf{x}))}{|\nabla(T(\mathbf{x}) + U(\mathbf{x}))|}, \tag{6}$$

i.e., the vector defining the direction of the gravity vector, the Eq. 5) becomes

$$\mathbf{v}(\mathbf{x}) \cdot \nabla(T(\mathbf{x}) + U(\mathbf{x})) = g(\mathbf{x}), \tag{7}$$

and after some rearrangement we get

$$\mathbf{v}(\mathbf{x}) \cdot \nabla(T(\mathbf{x})) = g(\mathbf{x}) - \mathbf{v}(\mathbf{x}) \cdot \nabla(U(\mathbf{x})) \quad \mathbf{x} \in \Gamma. \tag{8}$$

Since the vector $\mathbf{v}(\mathbf{x})$ is unknown and depends on $T(\mathbf{x})$, BC (8) is still nonlinear, but its form allows to use an iterative approach for determining $\mathbf{v}(\mathbf{x})$ and $T(\mathbf{x})$ such that BVP defined as (1) - (3) is fulfilled.

Then the iterative procedure for solving NSFGBVP is defined as follows

$$\Delta T^{n+1}(\mathbf{x}) = 0 \quad \mathbf{x} \in \Omega, \tag{9}$$

$$\mathbf{v}^n(\mathbf{x}) \cdot \nabla(T^{n+1}(\mathbf{x})) = g(\mathbf{x}) - \mathbf{v}^n(\mathbf{x}) \cdot \nabla(U(\mathbf{x})) \quad \mathbf{x} \in \Gamma, \tag{10}$$

$$T^{n+1}(\mathbf{x}) = T_{SAT}(\mathbf{x}) \quad \mathbf{x} \in \partial\Omega - \Gamma, \tag{11}$$

for $n = 0, 1, 2, \ldots$, where

$$\mathbf{v}^n(\mathbf{x}) = \frac{\nabla(T^n(\mathbf{x}) + U(\mathbf{x}))}{|\nabla(T^n(\mathbf{x}) + U(\mathbf{x}))|}. \tag{12}$$

We start the iterations by choosing $T^0(\mathbf{x}) = 0$ and consequently for $\mathbf{v}^0(\mathbf{x})$ we get

$$\mathbf{v}^0(\mathbf{x}) = \frac{\nabla(U(\mathbf{x}))}{|\nabla(U(\mathbf{x}))|} = \mathbf{s}(\mathbf{x}), \tag{13}$$

where $\mathbf{s}(\mathbf{x})$ represents the direction of the normal gravity vector. In this way, in every iteration we solve the geodetic BVP for $T^{n+1}(\mathbf{x})$ with the prescribed oblique derivative vector $\mathbf{v}^n(\mathbf{x})$, while in the first one it is given by

$$\mathbf{s}(\mathbf{x}) \cdot \nabla(T^1(\mathbf{x})) = g(\mathbf{x}) - \gamma(\mathbf{x}) = \delta g(\mathbf{x}), \tag{14}$$

where $\gamma(\mathbf{x}) = |\nabla(U(\mathbf{x}))|$ denotes a magnitude of the normal gravity vector and $\delta g(\mathbf{x})$ stands for the gravity disturbance.

In the following iterations, we improve the direction of the unit vector $\mathbf{v}(\mathbf{x})$ and so reduce the linearization error. To stop the iteration process, we use as a criterion the difference between two successive iterations and stop the procedure, if in each point we get

$$|T^n(\mathbf{x}) - T^{n+1}(\mathbf{x})| < \varepsilon, \tag{15}$$

where ε is a user-specified small real number. Then the last iteration represents the approximation of the disturbing potential $T(\mathbf{x})$ and direction of gravity vector $\mathbf{v}(\mathbf{x})$ in (1) - (3), and the sum $T^{n+1}(\mathbf{x}) + U(\mathbf{x})$ represents the approximation of actual gravity potential $W^{n+1}(\mathbf{x})$ in every point of the computational domain Ω.

3 The FEM solution to the nonlinear satellite-fixed geodetic BVP

We can see that in each step of our iterative process (9) - (11) we deal with the oblique derivative BVP defined as

$$\Delta T(\mathbf{x}) = 0 \quad \mathbf{x} \in \Omega, \tag{16}$$

$$\mathbf{v}(\mathbf{x}) \cdot \nabla(T(\mathbf{x})) = g(\mathbf{x}) - \mathbf{v}(\mathbf{x}) \cdot \nabla(U(\mathbf{x})) = \alpha(\mathbf{x}), \quad \mathbf{x} \in \Gamma, \tag{17}$$

$$T(\mathbf{x}) = T_{SAT}(\mathbf{x}) \quad \mathbf{x} \in \partial\Omega - \Gamma. \tag{18}$$

To solve (16) - (18), we apply the FEM, see (Brenner and Scott 2002) or (Reddy 2006). Since the boundary Γ, i.e., the discretized Earth's surface is complicated and irregular,

it is natural to choose triangular prisms, namely the finite pentahedral element Ω^e with six nodes and five faces. We discretize the whole computational domain Ω into n_1, n_2, n_3 elements in latitudinal, longitudinal and height direction, respectively. Then to specify the position of an element Ω^e we use indices k, l, m, where $k = 1, ..., n_1$, $l = 1, ..., n_2$ and $m = 1, ..., n_3$.

Let us consider an arbitrary element Ω^e from our finite element distretization with indices $k = 1, ..., n_1, l = 1, ..., n_2$ and $m = 2, ..., n_3$. We multiply (16) by a weight function w and using Green's identity (we omit ($\mathbf{x}$) to simplify the notation in the following equations) we obtain the weak formulation of (16) over an arbitrary above-defined element Ω^e

$$\int_{\Omega^e} \nabla T \cdot \nabla w \, \mathrm{d}x\mathrm{d}y\mathrm{d}z = \int_{\partial\Omega^e} \nabla T \cdot \mathbf{n}\, w \, \mathrm{d}\sigma, \tag{19}$$

where $\mathbf{n}$ denotes the unit normal to $\partial\Omega^e$.

Due to the oblique derivative BC (17) prescribed on the bottom boundary Γ, we derive the weak formulation for elements with indices $k = 1, ..., n_1, l = 1, ..., n_2$ and $m = 1$ separately. We follow the idea of Macák et al. (2020) or Minarechová et al. (2021). We split the oblique vector $\mathbf{v}$ into one normal, $\mathbf{n}$, and two tangential, $\mathbf{t}_1$, $\mathbf{t}_2$, components, and we insert this decomposition into (17)

$$\nabla T \cdot \mathbf{v} = c_1 \nabla T \cdot \mathbf{n} + c_2 \nabla T \cdot \mathbf{t}_1 + c_3 \nabla T \cdot \mathbf{t}_2 = \alpha. \tag{20}$$

From (20) we express the normal derivative

$$\nabla T \cdot \mathbf{n} = \frac{\alpha}{c_1} - \frac{c_2}{c_1}\frac{\partial T}{\partial \mathbf{t}_1} - \frac{c_3}{c_1}\frac{\partial T}{\partial \mathbf{t}_2}, \tag{21}$$

where $\partial T/\partial\mathbf{t}_1$ and $\partial T/\partial\mathbf{t}_2$ denote derivatives of the disturbing potential in the direction of $\mathbf{t}_1$ and $\mathbf{t}_2$, respectively, moreover we assume that $c_1 \neq 0$, and we insert (21) to (19) to get

$$\int_{\Omega^e} \nabla T \cdot \nabla w \, \mathrm{d}x\mathrm{d}y\mathrm{d}z =$$
$$= \int_{\Gamma^e} \left(\frac{\alpha}{c_1} - \frac{c_2}{c_1}\frac{\partial T}{\partial \mathbf{t}_1} - \frac{c_3}{c_1}\frac{\partial T}{\partial \mathbf{t}_2} \right) w \, \mathrm{d}\sigma + \int_{\partial\Omega^e\backslash\Gamma^e} \nabla T \cdot \mathbf{n}\, w \, \mathrm{d}\sigma. \tag{22}$$

After some rearrangement, we obtain

$$\int_{\Omega^e} \nabla T \cdot \nabla w \, \mathrm{d}x\mathrm{d}y\mathrm{d}z + \frac{c_2}{c_1}\int_{\Gamma^e} \frac{\partial T}{\partial \mathbf{t}_1} w \, \mathrm{d}\sigma + \frac{c_3}{c_1}\int_{\Gamma^e} \frac{\partial T}{\partial \mathbf{t}_2} w \, \mathrm{d}\sigma =$$
$$= \int_{\Gamma^e} \frac{\alpha}{c_1} w \, \mathrm{d}\sigma + \int_{\partial\Omega^e\backslash\Gamma^e} \nabla T \cdot \mathbf{n}\, w \, \mathrm{d}\sigma, \tag{23}$$

where $\mathbf{n}$ is the normal vector and $\mathbf{t}_1$, $\mathbf{t}_2$ are tangent vectors to $\Gamma^e \subset \partial\Omega^e \subset R^3$, where Γ^e denotes the bottom boundary of an element Ω^e.

Then for a pentahedral element Ω^e with six nodes we can write

$$T \approx T^e = \sum_{j=1}^{6} T_j^e \psi_j, \tag{24}$$

i.e. we approximate the unknown value T as T^e using a linear combination of basis functions ψ_j with coefficients T_j^e, $j = 1, ..., 6$. We substitute (24) into the weak formulation (19) and consider ψ_i for weight function w. We obtain the ith equation in the form

$$\sum_{j=1}^{6} T_j^e \int_{\Omega^e} \left(\frac{\partial \psi_j}{\partial x} \frac{\partial \psi_i}{\partial x} + \frac{\partial \psi_j}{\partial y} \frac{\partial \psi_i}{\partial y} + \frac{\partial \psi_j}{\partial z} \frac{\partial \psi_i}{\partial z} \right) \mathrm{dxdydz} =$$
$$= \sum_{j=1}^{6} \int_{\partial \Omega^e} q_n \, \psi_i \, \mathrm{dxdy}, \tag{25}$$

where $\partial \psi / \partial x$, $\partial \psi / \partial y$, $\partial \psi / \partial z$ are directional derivatives, $q_n = \nabla T \cdot \mathbf{n}$ denotes the projection of the vector ∇T along the unit normal $\mathbf{n}$.

For the row of elements Ω^e given by indices $k = 1, ..., n_1$, $l = 1, ..., n_2$ and $m = 1$, we follow the same way and after inserting (24) into (23) and considering $w = \psi_i$, we obtain the ith equation in the form

$$\sum_{j=1}^{6} T_j^e \left[\int_{\Omega^e} \left(\frac{\partial \psi_j}{\partial x} \frac{\partial \psi_i}{\partial x} + \frac{\partial \psi_j}{\partial y} \frac{\partial \psi_i}{\partial y} + \frac{\partial \psi_j}{\partial z} \frac{\partial \psi_i}{\partial z} \right) \mathrm{dxdydz} \right] +$$
$$+ \sum_{j=1}^{3} T_j^e \left(\frac{c_2}{c_1} \int_{\Gamma^e} \frac{\partial \psi_j}{\partial \mathbf{t}_1} \psi_i \, \mathrm{dxdy} + \frac{c_3}{c_1} \int_{\Gamma^e} \frac{\partial \psi_j}{\partial \mathbf{t}_2} \psi_i \, \mathrm{dxdy} \right) =$$
$$= \sum_{j=1}^{3} \int_{\Gamma^e} \frac{\alpha_j}{c_1} \psi_i \, \mathrm{dxdy} + \sum_{j=1}^{6} \int_{\partial \Omega^e \setminus \Gamma^e} q_n \, \psi_i \, \mathrm{dxdy}, \tag{26}$$

where index $j = 1, ..., 3$ refers to nodes of the element Ω^e that lie on the bottom boundary Γ of the computational domain Ω.

Now we can write (25) and (26) in a compact matrix form

$$\mathbf{K}^e \, \mathbf{T}^e = \mathbf{Q}^e, \tag{27}$$

where $\mathbf{K}^e = [K_{ij}]$ denotes the element stiffness matrix, $\mathbf{T}^e = (T_1, ..., T_6)$ is a column vector of unknowns and $\mathbf{Q}^e$ denotes the right-hand side vector.

To evaluate $\mathbf{K}^e$ and $\mathbf{Q}^e$ we proceed in the following way. We choose one basis function ψ_i per vertex N_i^e, see (Reddy 2006) or (Brenner and Scott 2002), and we differentiate the basis functions with respect to a position of each node in cartesian coordinates. To evaluate boundary integrals over a boundary Γ^e in (26), we approximate tangential derivatives like in the finite difference method. This idea has been applied also in Macák et al. (2020); Minarechová et al. (2021).

Afterwards, we assemble all element equations using two principles (Reddy 2006), namely "continuity of primary variables at the interelement nodes" and "balance of secondary variables in a weighted-integral sense at the interface between two elements", and we take into account the Dirichlet BC (18) for nodes that lie on the $\partial \Omega - \Gamma$. We have

obtained the global linear system of equations with a column vector of unknown global nodal values **T**

$$\mathbf{KT} = \mathbf{Q}, \tag{28}$$

where the matrix **K** is sparse and positive definite, and entries of the column vector **Q** are zeros except for the nodes with the prescribed BC (17).

4 Testing numerical experiment

To test and study the behaviour of the proposed numerical scheme, we performed one theoretical experiment. In this simplified testing case, the disturbing field was generated between two identical homogeneous spheres with the radius $R = 6378 \, [km]$ but with centers mutually shifted by $100 \, [km]$ in the direction of the z-axis, see Fig. 2, where the black sphere, denoted by S, represents the simplified "Earth" and the red sphere, denoted by S^*, the "normal body". Then the computational domain was bounded by latitude 80°S and 80°N, longitude 0° and 160° and the upper boundary has been placed at the altitude of $240 \, [km]$ above S. The generated gravitational potential, used to obtain the Dirichlet BC and the exact solution of (1), was calculated as GM/r, where GM denotes the geocentric gravitational constant and r denotes the distance from the origin O or O^*. To obtain BC on the bottom boundary, we used the derivative of this exact solution in the form $-GM/r^2$. We started (see Table 1) with the resolution $81 \times 41 \times 11$, i.e. with the number of nodes in longitudinal, latitudinal and radial direction, respectively. Afterwards, we performed four successive refinements and in each refinement we have calculated four iterations. We can see that with the refinement, we obtained the convergence of the method, and moreover it is obvious that the second iteration of our solution is very close to the "reference" value (see Table 1), so the following iterations bring only small improvement of the results. In this case, the "reference" value is used to designate

Fig. 2 The testing numerical experiment - the disturbing potential is obtained as a difference between the gravitational potential generated by the sphere S, representing the simplified Earth and depicted by black colour, and the gravitational potential generated by sphere S^* representing the normal body and depicted by red colour
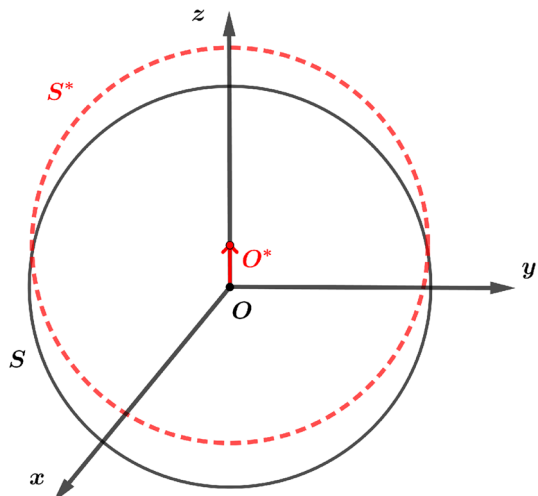
Table 1 Statistics of residuals between the FEM solution and the exact solution on the bottom boundary in the testing experiment (units: $m^2 s^{-2}$)

No. of nodes	No. of it	Min	Max	Mean	St. deviation
$81 \times 41 \times 11$	1	0.0000	1521.5100	968.5280	466.2330
	2	− 90.0984	102.0790	2.2471	58.0754
	3	− 90.2256	101.8830	2.2131	58.0730
	4	− 90.2256	101.8830	2.2131	58.0730
	Reference	− 90.1907	101.8410	2.2131	58.0729
$161 \times 81 \times 21$	1	0.0000	898.8630	569.7670	266.1540
	2	− 20.5623	23.2282	0.5822	14.6225
	3	− 20.5749	23.2025	0.5717	14.6219
	4	− 20.5749	23.2025	0.5717	14.6219
	Reference	− 20.5746	23.2021	0.5717	14.6219
$321 \times 161 \times 41$	1	0.0000	588.4360	363.7640	175.6500
	2	− 5.1203	5.7858	0.1485	3.6690
	3	− 5.1239	5.7783	0.1450	3.6680
	4	− 5.1239	5.7783	0.1450	3.6680
	Reference	− 5.1238	5.7782	0.1450	3.6678
$641 \times 321 \times 81$	1	0.0000	433.3740	259.1610	132.6990
	2	− 1.2796	1.4463	0.0378	0.9187
	3	− 1.2807	1.4438	0.0365	0.9187
	4	− 1.2807	1.4438	0.0365	0.9187
	Reference	− 1.28071	1.4438	0.0365	0.9187
$1281 \times 641 \times 161$	1	0.0000	355.8600	206.4710	111.7940
	2	− 0.3198	0.3619	0.0099	0.2300
	3	− 0.3201	0.3610	0.0091	0.2299
	4	− 0.3201	0.3610	0.0091	0.2299
	Reference	− 0.3201	0.3610	0.0091	0.2299

The "Reference" values are obtained with exactly calculated vector v(x) (see Eq. (17))

the values obtained with the exactly calculated vector **v(x)** (see eq. (17)), so this value includes only the discretization error.

5 High-resolution local gravity field modelling

We applied the developed concept to local gravity field modelling in three areas, namely the Andean, Himalayan and Alpine mountain range, where we expected a significant contribution of our approach due to rugged mountain terrain. In all three experiments, the input surface gravity disturbances were interpolated from Global Gravity Model plus

database (GGMPlus) (Hirt et al. 2013) on land areas and complemented by DTU21_GRAV data (Andersen and Knudsen 2019) on marine areas. The bottom surface was the discretized Earth's surface created from a digital elevation model provided within the GGMPlus database. The upper boundary was placed at the altitude of 230 km above the reference ellipsoid that corresponds to the mean altitude of the GOCE satellite orbits. The disturbing potential on the side boundaries and top boundary was generated from EIGEN-6C4 model (Förste et al. 2014), that is a static combined GGM up to d/o 2190. To solve the nonsymmetric linear system, BiCGSTAB(l) linear solver with $l = 8$, cf. (Sleijpen and Fokkema 1993), was implemented and the stopping criterion was set to 10^{-8}. To save memory, we stored only nonzero coefficients. All these large-scale parallel computations were performed on 4 nodes of our cluster with 1.0 TB of distributed memory (each node consists of four 8-core CPUs with 256 GB RAM). Thanks to the NUMA (Non-Uniform Memory Access) architecture of each node, we implemented a hybrid parallelization and the NUMA optimization using 32 MPI processes, each with 4 OpenMP threads (together 128 cores).

5.1 The Andean mountain range

The computational domain Ω for the Andean mountain range is bounded by longitude 278° and 300°, and by latitude 56°S and 12°N. The meshing was set to the number of division: $1100 \times 3400 \times 300$ (longitude x latitude x height) creating 1 127 094 801 nodes, including 3 744 501 nodes on the Earth's surface. These nodes formed 2 244 000 000 pentahedral elements. The corresponding horizontal resolution on the Earth's surface was $0.02° \times 0.02°$. A numerical solution of NSFBVP using the developed FEM approach on such a 3D unstructured mesh took about 15 h of the CPU time. Since the residuals between the third and the second iteration were smaller than 0.00001 $[m^2 s^{-2}]$, see Fig. 3d) and Table 2, we stopped our computation after the third iteration. The obtained numerical solution with the differences between two successive solutions is depicted in Fig. 3. One can observe that the highest values of differences are in the areas with the highest values of deflection of vertical and they reach up to -0.0571 $[m^2 s^{-2}]$ in the disturbing potential which corresponds approximately to 5.7 [mm] in the quasigeoidal height, see Table 2.

5.2 The Himalayan mountain range

The computational domain Ω for the experiment in Himalayan region is between 60°E and 110°E longitude, and bounded by latitude 20°N and 50°N. The meshing was set to: $2000 \times 1200 \times 320$ (longitude x latitude x height) creating 771 427 521 nodes, including 2 403 201 nodes on the Earth's surface. In this way, we obtained 1 536 000 000 pentahedral elements. The horizontal resolution on the Earth's surface has been $0.025° \times 0.025°$. The computation (i.e. all three solutions) took about 8,5 h of the CPU time. The obtained
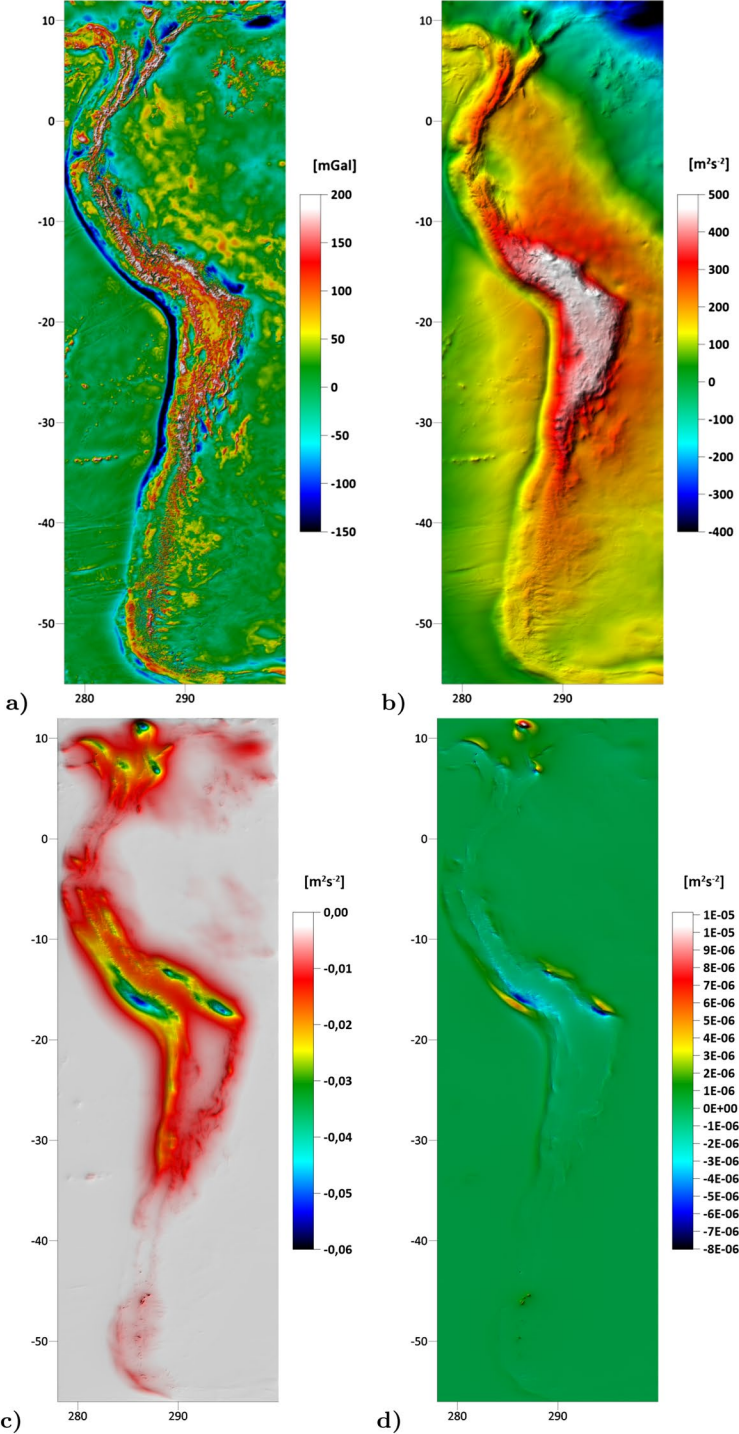
◄ **Fig. 3** *The Andean mountain range*: **a** The input surface gravity disturbances [*mGal*]; **b** The disturbing potential solution T^{1st} [m²s⁻²]; **c** The contribution of the second iteration, i.e. $(T^{2nd} - T^{1st})$ [m²s⁻²], where T^{2nd} denotes the disturbing potential solution after the second iteration; **d** The contribution of the third iteration, i.e. $(T^{3rd} - T^{2nd})$ [m²s⁻²], where T^{3rd} denotes the disturbing potential solution after the third iteration

Table 2 *Andean mountain range*: Statistics of residuals [m²s⁻²] between the second iteration T^{2nd} and the first iteration denoted by T^{1st}, and the third T^{3rd} and the second T^{2nd} iteration obtained on the bottom boundary Γ. STD denotes the standard deviation of residuals

Residuals	Min	Max	Mean	Median	STD
$T^{2nd} - T^{1st}$	− 0.0571	0	−0.0048	−0.0025	0.0063
$T^{3rd} - T^{2nd}$	− 8.03e−06	1.12e−05	1.02e−08	2e−08	4.91e−07

solution with the differences between two successive solutions is depicted in Fig. 4. The corresponding statistics is presented in Table 3. One can observe that the highest values of differences are again in the areas of the steepest changes of the disturbing potential, with values up to −0.0702 [m²s⁻²], see Table 3, which corresponds approximately to 7.0 [mm] in the quasigeoidal height. (Table 4)

5.3 The Alps mountain range

The computational domain Ω for the last experiment located in Alps region is bounded by longitude 4.799°E and 17.503°E, and by latitude 42.999°N and 49.203°N, see Fig. 5. The horizontal resolution on the Earth's surface was 0.004° × 0.004°, while the number of divisions in radial direction was set to 600. The total number of nodes in the computational domain was 2 963 353 104, including 4 930 704 nodes on the earth's surface, and forming 5 911 171 200 pentahedral elements. Again, based on the differences obtained between the third and the second iteration, see Table 3, we stopped the computation after the third iteration. The highest values of differences in the disturbing potential have been approximately −0.0066 [m²s⁻²], i.e. approximately to 0.6 [mm] in the quasigeoidal height, see Table 3 and Fig. 5.

6 Conclusion and summary

We developed an iterative approach based on the finite element method applied for solving the nonlinear satellite-fixed geodetic boundary value problem. In this concept, we determined the direction of actual gravity vector together with the value of the disturbing potential. To solve it, we implemented the finite element method with triangular prisms. For the numerical experiments we chose three mountainous locations, namely in Andean, Himalayan and Alpine mountain ranges. As an input data we used the surface gravity disturbances generated from Global Gravity Model plus database
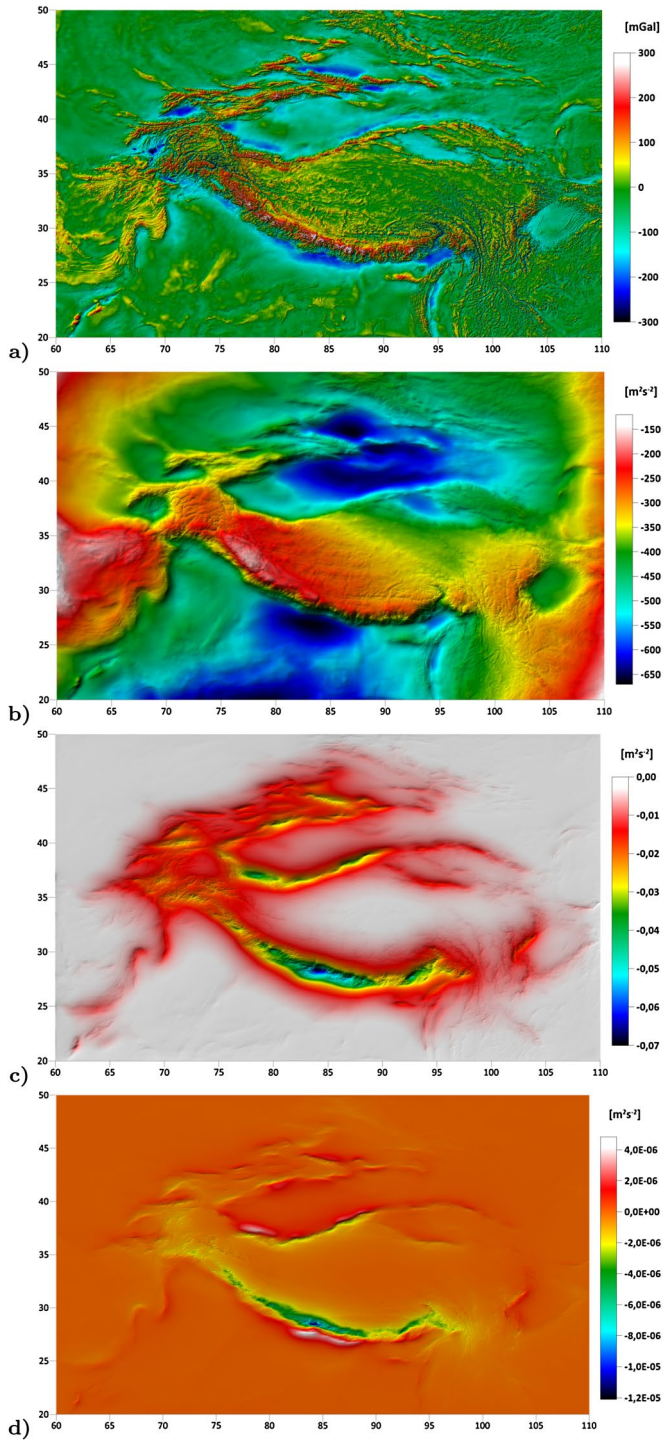
◀ **Fig. 4** *The Himalayan mountain range*: **a** The input surface gravity disturbances [*mGal*]; **b** The disturbing potential solution T^{1st} [m²s⁻²]; **c** The contribution of the second iteration, i.e. $(T^{2nd} - T^{1st})$ [m²s⁻²], where T^{2nd} denotes the disturbing potential solution after the second iteration; **d** The contribution of the third iteration, i.e. $(T^{3rd} - T^{2nd})$ [m²s⁻²], where T^{3rd} denotes the disturbing potential solution after the third iteration

Table 3 *Himalayan mountain range*: Statistics of residuals [m²s⁻²] between the second iteration T^{2nd} and the first iteration denoted by T^{1st}, and the third T^{3rd} and the second T^{2nd} iteration obtained on the bottom boundary Γ

Residuals	Min	Max	Mean	Median	STD
$T^{2nd} - T^{1st}$	−0.0702	0	−0.0066	−0.0040	0.0070
$T^{3rd} - T^{2nd}$	−1.58e−05	4.84e−06	−8.93e−08	−1e−08	5.80e−07

Table 4 *The Alps*: Statistics of residuals [m²s⁻²] between the second iteration T^{2nd} and the first iteration denoted by T^{1st}, and the third T^{3rd} and the second T^{2nd} iteration obtained on the bottom boundary Γ

Residuals	Min	Max	Mean	Median	STD
$T^{2nd} - T^{1st}$	−0.0066	0	−0.0012	−0.0008	0.0011
$T^{3rd} - T^{2nd}$	-1.3e−07	1.9e−07	6.1e−09	0	2.4e−08

(lands) combined with DTU21_GRAV model (seas), and the disturbing potential generated from EIGEN-6C4 model. The obtained maximal contribution to disturbing potential when taking into account the nonlinear boundary condition with comparison to the oblique derivative boundary condition was 0.0571 [m²s⁻²] (Andes), 0.0702 [m²s⁻²] (Himalayas), 0.0066 [m²s⁻²] (Alps). These values correspond to 5.7 [mm] (Andes), 7.0 [mm] (Himalayas), 0.6 [mm] (Alps) in the quasigeoidal heights, and they are located in the areas of the highest values of the deflection of vertical. The obtained results confirm the validity of the presented approach.
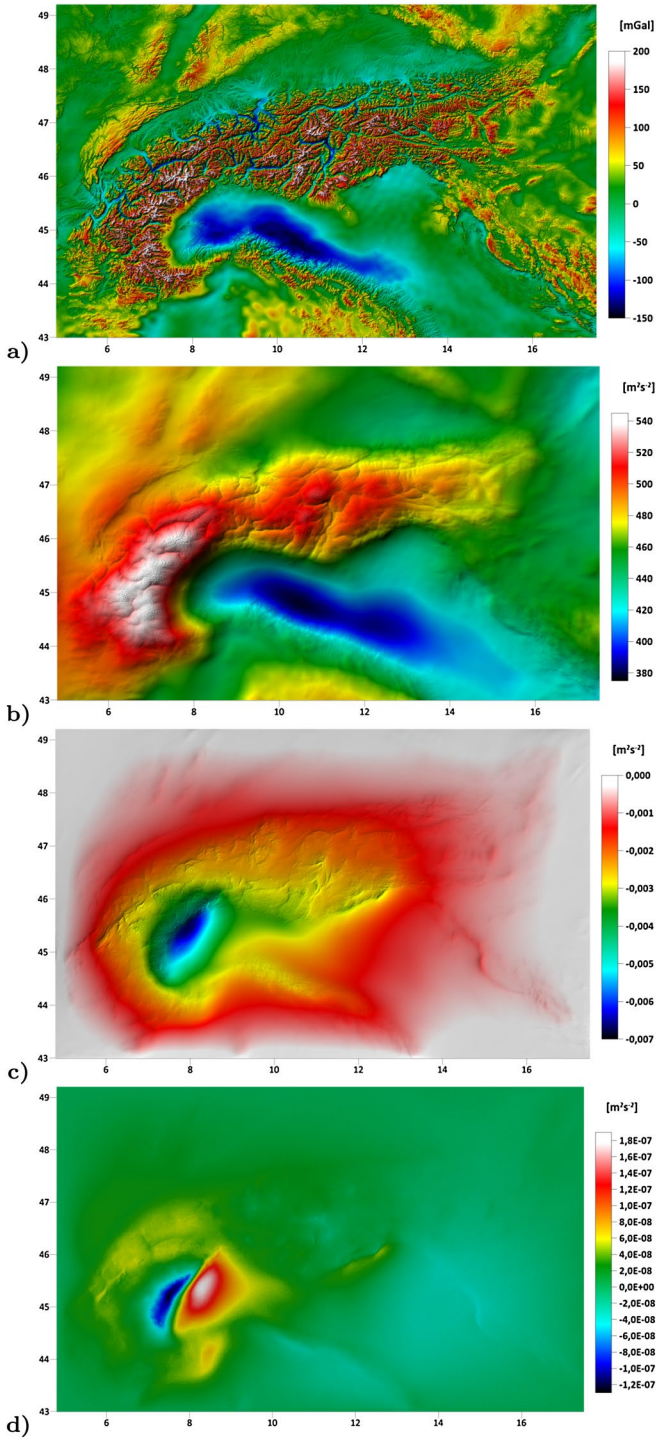
◀ **Fig. 5** *The Alps mountain range*: **a** The input surface gravity disturbances [*mGal*]; **b** The disturbing potential solution T^{1st} [m^{2}s^{-2}]; **c** The contribution of the second iteration, i.e. $(T^{2nd} - T^{1st})$ [m^{2}s^{-2}], where T^{2nd} denotes the disturbing potential solution after the second iteration; **d** The contribution of the third iteration, i.e. $(T^{3rd} - T^{2nd})$ [m^{2}s^{-2}], where T^{3rd} denotes the disturbing potential solution after the third iteration

Data availability All datasets generated and/or analysed within the experiments are available from the corresponding author.

Declarations

Conflict of interests All authors declare that they have no conflicts of interest.

References

Andersen OB, Knudsen P (2019) The DTU17 Global marine gravity field: First Validation Results. In: Mertikas S, Pail R (eds) Fiducial Reference Measurements for Altimetry. International Association of Geodesy Symposia, vol 150. Springer, Cham. https://doi.org/10.1007/1345_2019_65

Backus GE (1968) Application of a non-linear boundary-value problem for Laplace's equation to gravity and geomegnetic intensity surveys. Q J Mech Appl Math 2:195–221

Becker JJ, Sandwell DT, Smith WHF, Braud J, Binder B, Depner J, Fabre D, Factor J, Ingalls S, Kim SH, Ladner R, Marks K, Nelson S, Pharaoh A, Trimmer R, Von Rosenberg J, Wallace G, Weatherall P (2009) Global bathymetry and elevation data at 30 arc seconds resolution: SRTM30 PLUS. Mar Geodesy 32(4):355–371

Bjerhammar A, Svensson L (1983) On the geodetic boundary value problem for a fixed boundary surface. A satellite approach. Bull Geod 57(1–4):382–393

Brenner SC, Scott LR (2002) The mathematical theory of finite element methods. Springer-Verlag, New York

Bruinsma S, Förste C, Abrikosov O, Lemoine J, Marty J, Mulet S, Rio M, Bonvalot S (2014) ESA's satellite-only gravity field model via the direct approach based on all GOCE data. Geophys Res Lett 41(21):7508–7514. https://doi.org/10.1002/2014GL062045

Bucha B, Janák J (2013) A MATLAB-based graphical user interface program for computing functionals of the geopotential up to ultra-high degrees and orders. Comput Geosci 56:186–196. https://doi.org/10.1016/j.cageo.2013.03.012

Díaz G, Díaz JI, Otero J (2006) On an oblique boundary value problem related to the Backus problem in geodesy. Nonlinear Anal Real World Appl 7:147–166

Díaz G, Díaz JI, Otero J (2011) Construction of the maximal solution of Backus' problem in geodesy and geomagnetism. Stud Geophys Geod 55(3):415–440

Fašková Z, Čunderlík R, Janák J, Mikula K, Šprlák M (2007) Gravimetric quasigeoid in Slovakia by the finite element method. Kybernetika 43(6):789–796

Fašková Z, Čunderlík R, Mikula K (2010) Finite element method for solving geodetic boundary value problems. J Geod 84(2):135–144

Förste Ch, Bruinsma SL, Abrikosov O, Lemoine JM, Marty JC, Flechtner F, Balmino G, Barthelmes F, Biancale R (2014) EIGEN-6C4 The latest combined global gravity field model including GOCE data up to degree and order 2190 of GFZ Potsdam and GRGS Toulouse. GFZ Data Services. https://doi.org/10.5880/icgem.2015.1

Grafarend E, Niemeier W (1971) The free nonlinear boundary value problem of physical geodesy. Bull Geod 101:243–261

Grafarend E (1989) The geoid and the gravimetric boundary value problem, Report N 18, The Royal Institute of Technology (Dep of Geod), Stockholm

Heck B (1989) On the non-linear geodetic boundary value problem for a fixed boundary surface. Bull Geod 63(1):57–67

Hirt C, Claessens SJ, Fecher T, Kuhn M, Pail R, Rexer M (2013) New ultra-high resolution picture of 1 earth's gravity field. Geophys Res Lett 40:4279–4283

Hofmann-Wellenhof B, Moritz H (2006) Physical geodesy, 2nd edn. Springer-Verlag, Vienna. https://doi.org/10.1007/978-3-211-33545-1

Holota P (1997) Coerciveness of the linear gravimetric boundary-value problem and a geometrical interpretation. J Geod 71:640–651

Koch KR, Pope AJ (1972) Uniqueness and existence for the geodetic boundary value problem using the known surface of the earth. Bull Geod 46:467–476

Macák M, Mikula K, Minarechová Z, Čunderlík R (2016) On an iterative approach to solving the nonlinear satellite-fixed geodetic boundary-value problem. IAGSymp 142:185–192

Macák M, Minarechová Z, Čunderlík R, Mikula K (2020) The finite element method as a tool to solve the oblique derivative boundary value problem in geodesy. Tatra Mt Math Publ 75(1):63–80

Macák M, Čunderlík R, Mikula K, Minarechová Z (2021) Computational optimization in solving the geodetic boundary value problems. Discrete Contin Dyn Syst 14(3):987–999

Minarechová Z, Macák M, Čunderlík R, Mikula K (2021) On the finite element method for solving the oblique derivative boundary value problems and its application in local gravity field modelling. J Geodesy 95:70

Pavlis NK, Holmes SA, Kenyon SC, Factor JK (2012) The development and evaluation of the earth gravitational model 2008 (EGM2008). J Geophys Res 117:B04406. https://doi.org/10.1029/2011JB008916

Reddy JN (2006) An introduction to the finite element method, 3rd edn. McGraw-Hill Education, New York

Sacerdote F, Sansó F (1989) On the analysis of the fixed-boundary gravimetric boundary-value problem. In: Sacerdote F, Sansó F, proceedings of the 2nd Hotine-Marussi symposium on mathematical geodesy, Pisa, Politecnico di Milano, 507–516

Sleijpen GLG, Fokkema DR (1993) Bicgstab (l) for linear equations involving unsymmetric matrices with complex spectrum, http://dspace.library.uu.nl/handle/1874/16827

Authors and Affiliations

Marek Macák[1] · Zuzana Minarechová[1] · Róbert Čunderlík[1] · Karol Mikula[1,2]

✉ Zuzana Minarechová
zuzana.minarechova@stuba.sk

Marek Macák
marek.macak@stuba.sk

Róbert Čunderlík
robert.cunderlik@stuba.sk

Karol Mikula
karol.mikula@stuba.sk

[1] Faculty of Civil Engineering, Slovak University of Technology, Radlinského 11, Bratislava 810 05, Slovakia

[2] Algoritmy:SK s.r.o., Šulekova 6, Bratislava 81106, Slovakia